Targeting cancer with small molecule pan-KRAS degraders

Popow, Johannes; Farnaby, William; Gollner, Andreas; Kofink, Christiane; Fischer, Gerhard; Wurm, Melanie

Published in:
Science

DOI:
10.1126/science.adm8684

Publication date:
2024

Submitted Manuscript: Confidential
Template revised November 2022

Title: Targeting cancer with small molecule pan-KRAS degraders

Authors:

Johannes Popow[†,1], William Farnaby[†,2,3], Andreas Gollner[†,1], Christiane Kofink[†,1], Gerhard Fischer[1], Melanie Wurm[1], David Zollman[2,3], Andre Wijaya[2,3], Nikolai Mischerikow[1], Carina Hasenoehrl[1], Polina Prokofeva[4], Heribert Arnhof[1], Silvia Arce-Solano[1], Sammy Bell[5], Georg Boeck[1], Emelyne Diers[3], Aileen B. Frost[2,3], Jake Goodwin-Tindall[3], Jale Karolyi-Oezguer[1], Shakil Khan[2,3], Theresa Klawatsch[1], Manfred Koegl[1], Roland Kousek[1], Barbara Kratochvil[1], Katrin Kropatsch[1], Arnel A. Lauber[1], Ross McLennan[2,3], Sabine Olt[1], Daniel Peter[1], Oliver Petermann[1], Vanessa Roessler[1], Peggy Stolt-Bergner[1], Patrick Strack[1], Eva Strauss[1], Nicole Trainor[3], Vesna Vetma[2,3], Claire Whitworth[3], Siying Zhong[3], Jens Quant[1], Harald Weinstabl[1], Bernhard Kuster[4], Peter Ettmayer[*,1], Alessio Ciulli[*,2,3]

Afiliations:

[1] Boehringer Ingelheim RCV GmbH & Co KG; 1221 Vienna, Austria.
[2] Centre for Targeted Protein Degradation, School of Life Sciences, University of Dundee; DD1 5JJ, Dundee, UK.
[3] Division of Biological Chemistry and Drug Discovery, School of Life Sciences, James Black Centre, University of Dundee; DD1 5EH Dundee, Scotland, U.K.
[4] Proteomics and Bioanalytics, School of Life Sciences, Technical University of Munich; 85354 Freising, Germany.
[5] Boehringer Ingelheim Pharmaceuticals Inc.; Ridgefield, CT 06877, USA.
[†] These authors contributed equally to this work
[*] Corresponding authors Email: a.ciulli@dundee.ac.uk; peter.ettmayer@boehringer-ingelheim.com

Abstract:

Despite the high prevalence of cancers driven by KRAS mutations, to date only the G12C mutation has been clinically proven to be druggable via covalent targeting of the mutated cysteine amino acid residue (*1*). However, in many cancer indications other KRAS mutations, such as G12D and -V, are far more prevalent and small molecule concepts that can address a wider variety of oncogenic KRAS alleles are in high clinical demand (*2*). Here we show that a single small molecule can be used to simultaneously and potently degrade 13 out of 17 of the most prevalent oncogenic KRAS alleles, including those not yet tractable by inhibitors. Compared with inhibition, degradation of oncogenic KRAS results in more profound and sustained pathway modulation across a broad range of KRAS mutant cell lines. As a result, KRAS degraders inhibit growth of the majority of cancer cell lines driven by KRAS mutations while sparing models without genetic KRAS aberrations. Finally, we demonstrate that pharmacological degradation of oncogenic KRAS leads to tumour regression in vivo. Together, these findings unveil a new path towards addressing KRAS driven cancers with small molecule degraders.

One-Sentence Summary:

The most prevalent KRAS variants which drive tumour growth in a major share of cancer patients can be targeted with a single small molecule degrader.

Main Text:

Introduction

Kirsten rat sarcoma viral oncogene homologue (KRAS) is the most commonly mutated oncogene in human cancers (*3*). Variants, predominantly mutations at Glycine (G) 12 or Glutamine (Q) 61, increase the proportion of activated, GTP-loaded KRAS, enhancing RAF-MEK-ERK (MAPK) signaling and drive tumor growth. To date, clinical advances in drugging oncogenic KRAS variants have relied on specific interactions of small molecules with the mutated amino acid residues. For example, covalent inhibitors rely on a cysteine residue available in $KRAS^{G12C}$ (*1, 4*) while reversible inhibitors rely on interactions between basic moieties and a variant specific aspartate residue in $KRAS^{G12D}$ (*5*). Indeed, beyond these variants, even pre-clinical target validation has been reliant on genetic means that lack dose, kinetic and temporal control. New concepts that can lead to single agents capable of potently and selectively addressing multiple KRAS variants stand to have major clinical impact. Recently, BI-2865 and BI-2493 were disclosed as the first example of KRAS inhibitors capable of engaging a broader spectrum of KRAS alleles than clinically validated inhibitors (*6*).

Small molecule heterobifunctional degraders (proteolysis targeting chimeras - PROTACs) are transforming drug development for oncology, with >25 degrader drugs in clinical trials for several indications (*7, 8*). Early PROTACs recruiting the von Hippel-Lindau (VHL) or cereblon E3 ubiquitin ligases to $KRAS^{G12C}$ have been disclosed based on covalent KRAS binders (*9, 10*). However, as KRAS engagement mediated by covalent target ligands itself leads to irreversible inhibition, this approach inherently lacks key mechanistic advantages of degraders such as substoichiometric and catalytic mode of action (*11*). To engage and degrade a wider range of KRAS variants beyond G12C, PROTAC degraders thus require leveraging of non-covalent KRAS binders, the discovery of which has proven inherently challenging. However, there has been recent progress in this direction, with non-covalent $KRAS^{G12D}$ degraders based on $KRAS^{G12D}$-selective inhibitors currently undergoing early clinical testing (*12*).

Here, we provide pre-clinical validation for a single small molecule degrader, targeting 13 of the 17 most prevalent KRAS mutants, which illuminates a new pan-KRAS degradation concept conferring potential for major clinical benefit. By employing structure-guided design we identify ACBI3, which achieves *in vivo* degradation of oncogenic KRAS, resulting in durable pathway modulation and tumour regressions in *KRAS* mutant xenograft mouse models.

Identification of VHL-based KRAS Degraders Based on Non-Covalent KRAS Binders

As a starting point, we chose to use a high affinity KRAS switch II pocket ligand we have recently disclosed (*6, 13*). Analysis of co-crystal structures highlighted a solvent exposed sub-pocket formed by the amino acids His95, Glu62, and Asp92, which we deemed to be a promising position to install linkers for PROTAC design (Fig. 1A). Due to the importance of the interaction of the basic center of these substituents with the surrounding amino acids we focused our PROTAC design approach on motifs maintaining the basicity of the molecule in this region. Thorough X-ray crystallographic analysis (PDB accession code 8QUG) of the recently published BI-2865 and close analogs revealed that the homopiperazine compound **1** (dissociation constant for $KRAS^{G12V}$ by surface plasmon resonance – SPR – K_D = 25 nM, table S1), provided a suitable trajectory for linker attachment (Fig. 1A). Applying an initial screening approach based on alkyl and polyethylene glycol (PEG)-based linkers in combination with VHL ligase binders based on VH032 (*14*), we tested the resulting molecules in a biophysical screening assay based on fluorescence polarization (FP). This assay reports affinity for the VHL:EloC:EloB (VCB) complex with or without pre-incubation

at saturating concentrations of $KRAS^{G12D}$. Cooperative VCB:PROTAC:$KRAS^{G12D}$ ternary complex formation is indicated by lower competitor concentrations achieving half maximal displacement (K_D) in the presence of $KRAS^{G12D}$ (*15*). This highlighted compound **2** (Fig. 1B) as a highly cooperative (alpha = 479, table S1) and high-affinity ternary complex inducer (K_D = 7 187 nM *vs* 15 nM in the absence or presence of $KRAS^{G12D}$, respectively) (Fig. 1C, table S1). We orthogonally confirmed ternary complex formation via SPR yielding a ternary complex dissociation half-life ($t_{1/2}$) of 159 s and an equilibrium dissociation constant (K_D) of 20 nM (Fig. 1D, table S1). Compound **2** dose-dependently degraded $KRAS^{G12D}$ in GP5d cells with a concentration inducing half maximal degradation (DC_{50}) at 24 hours of 607 nM and a maximal extent of degradation (D_{max}) of >95% (Fig. 1E, table S2). Similar results were obtained by Western blotting using an antibody detecting both wild type and mutant KRAS expressed by GP5d cells (fig. S1A). Compound **2** also degraded $KRAS^{G12V}$ in SW620 cells (DC_{50} = 1 203 nM, D_{max} >95%) indicating that KRAS degradation is not limited to $KRAS^{G12D}$ (fig. S1B, table S2). To enable high throughput characterization of degraders, we set up a bioluminescence-based degradation assay in GP5d cells expressing $KRAS^{G12D}$ with a small luminescence complementation (HiBiT) tag inserted into the endogenous KRAS locus yielding comparable degradation parameters (fig. S1C, table S2) (*16*). Degradation was abolished in the presence of the NEDD8-activating enzyme inhibitor MLN4924 (*17*) or the competing VHL ligand VH298 (*18*) (fig. S1D) supporting that KRAS degradation by compound **2** depends on intracellular recruitment of an active VHL ligase complex. We also detected direct KRAS ubiquitination and intracellular formation of ternary complexes by bioluminescence resonance energy transfer (BRET) based assays (fig. S1E and -F). The cellular target engagement assays, comparing the ability of compound **2** to engage VHL in either permeabilized or live cells (IC_{50} values 5 µM and >10 µM, respectively) indicated the need to further optimize cellular permeability as well as VHL affinity (Fig. 1F).

Having established compound **2** as a VHL-based KRAS degrader, we went on to synthesize a molecular matched pair, replacing the oxygen atom in the linker by a methylene group yielding compound **3** (Fig. 1B). Compound **3** still displayed positive cooperativity and long-lived ternary complex half-life (alpha = 17, K_D = 340 nM by FP, K_D = 80 nM and $t_{1/2}$ = 103 s by SPR, Fig. 1C, fig. S1G, table S1) albeit reduced compared to compound **2**. Degradation potency improved by greater than ten-fold for $KRAS^{G12D}$ (GP5d, DC_{50} = 32 nM, D_{max} = 99%) (Fig. 1E, table S2) and $KRAS^{G12V}$ (SW620, DC_{50} = 278 nM, D_{max} = 88%) (fig. S1B, table S2) with similar results again obtained by Western blotting using an antibody detecting both wild type and mutant KRAS and loss of degradation at high concentrations favoring binary rather than ternary engagement, referred to as “hook effect” (fig. S1A). Cellular target engagement assays showed that both improved cellular permeability as well as VHL affinity likely contributed to the superior degradation potency of compound **3** (Fig. 1F). Selective targeting of KRAS while sparing H- and NRAS has been linked to the therapeutic window of the KRAS ligand we based our design upon (*6*). We therefore tested selectivity of degradation by targeted proteomics in the cell line NCI-H358. While we detected degradation of both $KRAS^{G12C}$ ($D_{max} \geq 54\%$) and $KRAS^{WT}$ ($D_{max} \geq 86\%$), which represents roughly one third of the KRAS pool in this cell line, we detected no significant change in H- or NRAS levels (Fig. 1G, fig. S1H).

To understand the binding mode and enable structure-based optimization, we determined the ternary co-crystal structure of compound **3** in complex with VCB and $KRAS^{G12V}$ at 2.2 Å resolution (Fig. 1H) (PDB 8QW6). Compound **3** adopts a “fishhook” conformation, burying the VHL binder section of compound **3** in a *de novo* binding interface formed between $KRAS^{G12V}$ and VHL. The crystal structure contains two molecules of ternary complex in the asymmetric unit, revealing a consistent binding mode (RMSD = 0.54 Å), but a different fingerprint of protein-protein and protein-ligand interactions. This indicates that there is subtle flexibility within the compound **3** ternary complex, allowing the complex to shift between nearby networks of favorable protein-protein interactions. Using a biophysics-

led screening approaching we identified compound **3** as a KRAS degrader prototype based on a non-covalent target ligand. However, we noted that compound **3** has a poorer efficiency of degradation for $KRAS^{G12C}$ as opposed to WT (Fig. 1G), motivating us to investigate if further improvements could be made to broaden the range of KRAS mutants we could potently degrade.

Identification of Pan-KRAS Degraders

With the objective of identifying molecules that potently degrade multiple KRAS mutants we next sought to employ structure-based design using the solved ternary co-crystal structure of compound **3** to improve ternary complex stability and intracellular VHL engagement. Extending ternary complex stability (increased $t_{1/2}$) has been shown to improve rate and potency of target protein degradation (*19-21*). Analysis of the VCB:compound **3**:$KRAS^{G12V}$ co-crystal structure (Fig. 1H) highlighted an opportunity to enhance interactions within the ternary complex by improving π-stacking between the exit vector amide of the VHL ligand and Tyr112. We therefore switched the amide for an isoxazole, which has been previously reported to improve VCB affinity in this position in other contexts (*22*), yielding compound **4** (Fig. 2A). A ternary complex co-crystal structure of VCB:compound **4:**$KRAS^{G12V}$ (PDB 8QW7) confirmed a consistent overall binding mode to that observed for compound **3** (RMSD = 0.72 Å), with compound **4** able to engage in π-stacking interaction between the isoxazole and Tyr112 of VCB as designed (Fig. 2B). As with compound **3**, the compound **4** ternary complex revealed different networks of induced protein-protein interactions within the two ternary molecules in the asymmetric unit, indicating complex flexibility. FP, SPR and cellular target engagement studies support a minor improvement in binary VHL engagement for compound **4**, with moderate cooperativity retained (fig. S2A-C, table S1). A larger shift in durability of ternary complex can be observed via SPR for compound **4** ($t_{1/2}$ = 230 s, table S1) *vs* compound **3** ($t_{1/2}$ = 103 s, table S1). We then investigated the impact of these structural changes on degradation kinetics in live HiBiT-tagged GP5d cells (fig. S3A-D). While maximal degradation rates (λ_{max}) did not vary significantly between compound **3** and compound **4** (approximately 0.5 1/hour for both compounds, table S2), the concentration inducing the half maximal cellular degradation rate ($Dmax_{50}$) was three-fold lower for compound **4** ($Dmax_{50}$ = 56 nM for compound **3** *vs* $Dmax_{50}$ = 17 nM for compound **4**) (Fig. 2C, table S2). The improved $Dmax_{50}$ for compound **4** translated into drastically improved cellular VHL-dependent degradation potencies of compound **4** *vs* compound **3** for endogenous $KRAS^{G12D}$ (GP5d, DC_{50} = 1 nM, D_{max} = 99.5%, table S1) and $KRAS^{G12V}$ (SW620, DC_{50} = 13 nM, D_{max} = 89%) (Fig. 2D, fig. S3E-G).

To gauge KRAS mutation specificity on a broader basis without contribution of potentially confounding factors, we established an isogenic series of cell lines transduced with retroviral constructs expressing the most prevalent KRAS mutants (isoform 4B) fused to a HiBiT-tag in GP5d cells. Analysis of clones isolated from the resulting cell pools revealed that up to 30-fold differences in expression of tagged KRAS did not affect degradation potency of compound **4** in this system (fig. S3H and I). Constructs of both KRAS isoforms (4A and 4B) were degraded with comparable potencies (fig. S3J). Dose titration revealed that compound **4** efficiently degraded 13 of the 17 most prevalent KRAS mutant alleles and $KRAS^{WT}$ with single digit nanomolar potency (Fig. 2E). Supporting this, we obtained comparable results for endogenous KRAS in cell lines expressing $KRAS^{G12S}$, -G12A, -G13D and -Q61H treated with compound **4** (Fig. 2F). KRAS mutants with a more complete loss of GTPase activity, such as $KRAS^{G12R}$ (DC_{50} = 45 nM, D_{max} = 59%) and -Q61L/K/R (DC_{50} > 470 nM D_{max} < 60%), were degraded less potently, consistent with the relative binary binding affinity to these KRAS mutants of the ligand class employed in this study (*6*). Together, these data are consistent with degradation of KRAS mutants with residual GTPase activity by engagement of the inactive, GDP-bound state. Compound **3** was associated with a similar

degradation spectrum albeit with reduced potency for all degradable mutants suggesting that the optimized potency of compound **4** *vs* compound **3** affected a broad spectrum of KRAS alleles (Fig. 2G). We went on to assess the cellular selectivity of compound **4**-induced KRAS degradation by unbiased MS-proteomics in GP2d cells, using compound **5**, a VHL binding deficient stereoisomer of compound **4** as a negative control. KRAS was the only detected protein showing > 2-fold depletion ($p < 0.01$) with NRAS levels not significantly affected (Fig. 2H). Similar results were obtained in $KRAS^{G12C}$ mutant MiaPaCa-2 cells using another VHL binding deficient isomer, compound **6** as a degradation deficient control (fig. S3K). In summary, our structure-guided design approach led us to compound **4**, a highly selective KRAS degrader now acting on a broad spectrum of KRAS mutants with high prevalence in cancer patients.

KRAS Degradation Potently Suppresses Oncogenic Signaling and Proliferation

Next, we set out to test the ability of a single pan-KRAS degrading molecule, compound **4**, to selectively suppress oncogenic signaling and proliferation in cancer cell lines driven by diverse KRAS mutants. To this end, we first confirmed degradation of KRAS by compound **4** in KRAS-dependent (GP2d, SW620 and NCI-H358 expressing $KRAS^{G12D}$, -G12V or -G12C, respectively) as well as in KRAS independent (A-375, HEK293) cell lines (Fig. 3A, fig. S4A). To compare degradation *vs* inhibition of KRAS, we also profiled compound **5** (VHL-binding deficient stereoisomer) which has the same overall chemical formula and close-to-identical physicochemical properties and engages KRAS non-covalently without inducing KRAS degradation (Fig. 3A, fig. S4A). Alongside, we also profiled the covalent inhibitor of $KRAS^{G12C}$ Sotorasib (*23*) or the non-covalent $KRAS^{G12D}$ inhibitor MRTX-1133 (*24*) as appropriate (Fig. 3A, fig. S4A). Both inhibition and degradation repressed the established markers of MAPK signaling pERK (fig. S4B-D) and *DUSP6* (Fig. 3B, fig. S4E) in KRAS dependent cell lines. Both KRAS independent cell lines did not exhibit suppression of pERK or *DUSP6* exceeding 50% of control (Fig. 3B, fig. S4B and D-E). Compound **4** was > 10-fold more potent in suppressing MAPK signalling in KRAS dependent cell lines compared to its VHL binding deficient stereoisomer compound **5** indicating that E3 ligase engagement and subsequent target degradation as compared to inhibition results in more potent pathway engagement (Fig. 3B, fig. S4B-E, table S2). In the KRAS-dependent cell lines MAPK pathway engagement coincided with prominent inhibition of proliferation, with degradation conferring a greater than ten-fold and up to 100-fold potency gain (Fig. 3C, fig. S4F, table S2). Neither degradation nor inhibition had appreciable antiproliferative effects in the KRAS independent cell lines A-375 and HEK293 (Fig. 3C, fig. S4F). Comparable results albeit with lower potency were obtained for compound **3** (fig. S5, table S2). While long term treatment with compound **4** sustainably suppressed mutant and wild type KRAS expression for up to 72 hours in *KRAS* mutant and $KRAS^{WT}$ cell lines (fig S6A-D, top row), we noted a pronounced recovery of phospho-protein markers of both the MAPK- and phosphoinositide kinase pathways in *KRAS* mutant cell lines for both KRAS degraders and -inhibitors (fig. S6A-C, second to third row). This observation suggests that reactivation via feedback mechanisms occurs in the presence of minimal levels of mutant KRAS possibly, at least in part mediated by H- and NRAS as suggested by H- and NRAS contributing to MAPK pathway output upon KRAS inhibition (*6*). *DUSP6* modulation and induction of apoptosis confirmed the greater than 10-fold potency gain for KRAS degradation over -inhibition (compare results for compound **4** and 10-fold excess of the degradation inactive stereoisomer compound **5** in fig S6A-C, fourth and fifth row). In agreement with KRAS mediating mitogenic signaling, both KRAS inhibition and degradation induced a prominent G1/G0 cell cycle arrest in *KRAS* mutant but not $KRAS^{WT}$ cell lines, with a greater than 10-fold potency gain for degradation *vs* inhibition (fig. S6A-D, bottom panels). Analogous to short term proliferation assays, clonogenic growth assays also support the

enhanced potency of KRAS degradation over KRAS inhibition in *KRAS* mutant but not *KRAS^{WT}* cell lines (fig. S6E-H).

Pharmacological degradation of a target can result in target resynthesis dependent pathway engagement (*25*). To test whether this applies to our KRAS degraders, we pre-treated KRAS^{G12D}-dependent GP2d cells with compound **4** to achieve maximal KRAS degradation or the inactive stereoisomer compound **5** at the identical concentration and 10-fold excess to achieve comparable pathway inhibition by non-covalent engagement of KRAS. After pre-incubation, the medium was exchanged to wash out compound **4** or its inactive stereoisomer and replaced by culture medium containing VH298 to compete against VHL binding of any residual compound **4** (Fig 3D, empty bars). Alternatively, we re-exposed the cells to the same treatments as during the pre-incubation (Fig. 3D, filled bars). Upon washout, KRAS^{G12D} levels recovered in a time-dependent fashion reaching 21% of untreated controls 24 hours after washout of compound **4**. In contrast, KRAS^{G12D} levels remained below 5% of controls upon re-addition of compound **4** (Fig. 3D, top panel, compare red empty bars with red solid bars, respectively). Both pERK and DUSP6 rapidly recovered after washout of the inactive stereoisomer compound **5** reaching control levels after 2-4 hours even though the 10-fold excess of compound **5** achieved pERK and DUSP6 suppression comparable to the compound **4** pre-incubation. In contrast, cells pre-treated with compound **4** exhibited long lasting MAPK pathway suppression consistent with the delayed recovery of KRAS^{G12D} after washout (Fig. 3D, middle and bottom panels, compare empty red bars with empty dark blue bars). Of note, re-addition of compound **4** or 1 µM compound **5** appreciably suppressed pERK and DUSP6 for up to 24 hours after media exchange and compound re-addition. Hence, KRAS degradation results in long-lasting MAPK pathway suppression with delayed recovery compared to non-covalent KRAS inhibition upon compound withdrawal. We also compared the antiproliferative activity of compound **4** to that of KRAS^{G12C}-specific covalent-, non-covalent KRAS- and the MEK inhibitor trametinib in a cell line panel comprising 300 cell lines covering a range of KRAS mutations and cancer indications (Fig. 3E). On a global scale, cell lines bearing KRAS mutants had lower concentrations required for half-maximal proliferation inhibition (IC_{50}) as compared to WT cell lines (geometric mean IC_{50} = 739 nM *vs* 4 934 nM, respectively) (fig. S6I). Applying a sensitivity cutoff of 1 µM, all sotorasib-sensitive *KRAS^{G12C}*-mutant cell lines were also sensitive to compound **4**. In addition, sensitivity to compound **4** was correlated with that of the KRAS inhibitor BI-2493 albeit with higher potency for compound **4**. Notably, most cell lines sensitive to compound **4** as well as BI-2493 bear a KRAS mutation whereas trametinib exhibits less selective antiproliferative effects and potently kills *KRAS^{WT}* cell lines (Fig. 3E, heat maps underneath bar plot). Consistent with the drastically reduced activity of compound **4** on highly hydrolysis impaired KRAS mutants, the two *KRAS^{Q61K}* mutant cell lines were insensitive (Fig. 3E, genetic features underneath bar plot). Apart from reasons pertaining to high-throughput antiproliferative activity profiling, some features may explain insensitivity of a subset of *KRAS* mutant cell lines to compound **4**. For instance, lack of antiproliferative activity of compound **4** in cell lines sensitive to KRAS ablation may be linked to its susceptibility to drug efflux (table S3, CaCo-2 assay). Co-treatment with the ABCB1 efflux-pump inhibitor Zosuquidar (*26*) rescued both proliferation and KRAS degradation in LS513 cells expressing high levels of ABCB1 (fig. S6J and K).

To characterize the effects of pan-KRAS degradation more globally on the molecular level, we performed a time-resolved (phospho-)proteomic analysis of NCI-H358 and GP2d cells in response to compound **4** or its VHL-binding deficient isomer compound **5** at the concentration of compound **4** achieving maximal degradation in each cell line (fig. S7A). The results recapitulated KRAS (but not HRAS) degradation in both models (fig. S7B and -C), and quantification of ~20 000 phosphorylation sites allowed for the comprehensive characterization of affected phosphorylation events (fig. S7D). Phosphorylation events detected in all treatments revealed a pronounced overlap for both compounds in either cell

line, with several cell line-specific differences (Fig. 3F). While both compound **4** and compound **5** engaged the MAPK pathway, compound **4** modulated phosphorylation events detected in all treatments with greater effect size than compound **5** (Fig. 3F, fig. S7E). Only a few phosphorylation events displayed more pronounced modulation by compound **5** as compared to compound **4** (Fig. 3F, fig. S7E). Gene ontology enrichment analysis demonstrated reduced activity of multiple pathways, including the cell cycle, in response to compound **4** but not compound **5** (Fig. 3G, fig. S7F and -G). Hence, both inhibition and degradation of KRAS modulate largely overlapping sets of phosphorylation events albeit with distinct effect size and potency. Taken together, as compared to target inhibition achieved by compounds with comparable molecular properties, KRAS degradation enables greater than 10-fold higher potency paired with extended and more pronounced suppression of MAPK signaling. In conclusion, KRAS degradation selectively shuts down oncogenic signaling more potently and more durably than a matched molecular pair inhibitor in KRAS dependent cell lines. This leads to suppression of cell cycle progression, induction of apoptosis and thus inhibition of proliferation in the context of a wide range KRAS mutants *in vitro*.

In Vivo KRAS Degradation leads to regressions in KRAS mutant tumor-bearing mice.

Next, we wished to understand possible advantages of KRAS degradation *in vivo*. For instance, degradation has been shown to extend pharmacodynamic (PD) efficacy beyond the detectable pharmacokinetic (PK) presence of a degrader in other settings (*25*). Pharmacokinetic profiling of compound **4** suggested insufficient exposure irrespective of the route of administration. Plasma concentrations achieved via intravenous (*i.v.*) or sub-cutaneous (*s.c.*) dosing did not cover the predicted *in vivo* DC_{50} (Fig. 4A, table S3 and S4). The latter was estimated using potency of degradation of HiBiT-labeled $KRAS^{G12D}$ in assays with fetal calf serum (FCS) substituted by serum of NMRI mice or human serum. Whereas the degradation potency of compound **4** was comparable in FCS and human serum (DC_{50} = 1.4 and 1.9 nM, respectively), we noted a 24-fold potency drop in presence of 10% mouse serum (DC_{50} = 33 nM) (Fig. 4B). This yields a predicted *in vivo* DC_{50} of 851 nM for the GP2d model in NMRI mice (*vs* 3.6 nM in FCS) (table S2).
Seeking to achieve *in vivo* active concentrations and to maintain the productive elements of ternary complex molecular recognition observed in compounds **3** and -**4**, we swapped the isoxazole for a triazole and introduced a hydroxymethyl group at the benzylic position of the VHL binder to obtain compound **7,** herein referred to as ACBI3 (Fig. 4C). While slightly improving solubility (4 µg/mL *vs* < 1 µg/mL at pH 4.5, table S3) SPR (fig. S8A) and FP (fig. S8B) suggested remarkable VHL engagement for ACBI3, with high signal detected via SPR beyond >1 000 s resulting in an apparent biophysical half-life of its binary complex with VHL of > 2 000 s (fig. S8A, table S1). Aiming to measure ternary complex stability, we noted that the FP assay reached the limits of quantification due to ternary K_D approaching that of the assay probe (fig. S8B). However, by SPR, ternary complex K_D was quantifiable and 4-fold improved *vs* compound **4** (6 nM for ACBI3 *vs* 26 nM for compound **4**) (fig. S8C, table S1). Single particle cryo-electron microscopic analysis of the $KRAS^{G12V}$:ACBI3:VCB:Cul2:Rbx1 complex (fig. S9 and S10) revealed significant flexibility throughout the entire complex (Fig. 4D), likely necessary for successful ubiquitin transfer. While high-resolution modelling of ACBI3 binding was limited by a high flexibility of KRAS, we clearly observed the density of the VHL-binding part of ACBI3, as well as the connecting density of the linker (fig. S11A and B). Overlay with a 2.2 Å resolution ternary co-crystal structure of $KRAS^{G12V}$:ACBI3:VCB (PDB 8QVU) supports the same overall binding architecture via both techniques (Fig. 4D, fig. S11C). Details of the PROTAC binding site in the X-ray structure were resolved revealing a flexible binding mode overall consistent with those of compound **3** and compound **4** (fig. S11D). ACBI3 maintains the triazole-Tyr112 π-stack as observed with the isoxazole of compound **4**, while engaging an

additional H-bond interaction between the newly incorporated benzylic hydroxy group and Gln99 in $KRAS^{G12V}$ (fig. S11D). Multiple strong protein-protein interactions were apparent in the crystal structure which differed between protomers, indicating that, as with compound **3** and compound **4,** ACBI3 ternary complexes can dynamically transition between different H-bond networks between VHL and $KRAS^{G12V}$.

ACBI3 exhibited potent intracellular VHL engagement, ternary complex formation and ubiquitination translating into potent E3-ligase dependent cellular degradation and proteome-wide selectivity comparable to compound **4** (fig. S12A-H, table S2). Similarly, kinetic degradation parameters of ACBI3 (fig. S12I-L, table S2) and KRAS allele degradation specificity (fig. S13A) were comparable to compound **4**. Testing the antiproliferative activity in a cell line panel revealed that ACBI3 was broadly active on *KRAS* mutant *vs* $KRAS^{WT}$ cell lines (geometric mean IC_{50} = 478 nM *vs* 8.3 µM, respectively) (fig. S13B). Similar to compound **4**, ACBI3 exhibited high efflux in the Caco-2 assay (table S3). Hence, we also tested the activity of ACBI3 in cell lines in the presence of Zosuquidar (fig S13C). Inhibition of drug efflux resulted in 1 000-fold increased antiproliferative potency of ACBI3 (Fig. 4E) but not the KRAS inhibitor BI-2493 (fig. S13D) in LS513, a cell line with high *ABCB1* expression. The overall sensitivity pattern in the cell line panel was comparable in the presence or absence of Zosuquidar (fig. S13B and C). On a global scale, we observed an average 5-fold shift in potency attributable to efflux transporter expression in KRAS mutant cell lines (fig. S13E). This analysis likely underestimates the full antiproliferative activity of both KRAS inhibition and degradation as several *KRAS* mutant cell lines display more prominent KRAS dependency under anchorage independent (3D) conditions (*6*) not amenable to the applied high-throughput approach employed here (fig S13F-G). We conclude that, in addition to compromising oral bioavailability, ABCB1-mediated efflux creates the need for compensation by higher doses of ACBI3 in ABCB1 expressing tumors.

To establish *in vivo* proof of concept, we formulated ACBI3, which lacks oral bioavailability, in PEG-400 / Transcutol / Kolliphor HS 15 (*27*) to enable multiple *s.c.* daily dosing studies with a delayed absorption profile. *S.c.* administration of 30 mg/kg ACBI3 in this formulation resulted in a plasma concentration-time-profile (Fig. 4F) covering the *in vivo* DC_{50} of 281 nM—predicted based on degradation potency shift assays (Fig. 4G) and the degradation potency of ACBI3 in GP2d cells in 10% FCS (DC_{50} = 3.9 nM) (table S2)—for around 6 hours. Administering ACBI3 to GP2d tumor bearing mice, we observed degradation of $KRAS^{G12D}$ (44% of untreated controls) in tumors consistent with exposures covering the DC_{50} for at least 6 hours *in vivo* (Fig. 4H and I). While exposures varied 5-fold between the 6 and 24 hours timepoints (Fig. 4H), $KRAS^{G12D}$ levels did not recover to a notable extent consistent with extending the pharmacodynamic efficacy beyond the pharmacokinetic presence of ACBI3 at concentrations covering the predicted *in vivo* DC_{50}. In an anti-tumor efficacy study in GP2d tumor bearing mice, 30 mg/kg ACBI3 dosed daily *s.c.* for up to 14 days resulted in pronounced tumor regressions (Fig. 4J) with a tumor growth inhibition of 127% and a significant difference of control *vs* treatment group ($p < 0.0001$). This demonstrates that the PROTAC mediated suppression of oncogenic KRAS observed *in vitro* translates into *in vivo* regressions in KRAS mutant tumor bearing mice. Pleasingly, we also noted no impact on body weight (fig. S13H) suggesting selective degradation of KRAS is systemically tolerated in mice. Of note, ACBI3 degrades murine KRAS *in vitro* and *in vivo* (Fig 4K and fig S13I and -J). While systemically well tolerated, we observed skin lesions in mice of *s.c.* efficacy studies and thus do not recommend further use of this formulation and route of administration for *in vivo* experiments. We therefore moved to intraperitoneal (*i.p.*) delivery of ACBI3 formulated as a nano-milled suspension which upon repeated dosing resulted in exposures covering the predicted *in vivo* DC_{50} for six hours and were tolerated (Fig. 4F). Attesting to the antitumor activity of ACBI3 beyond a single KRAS mutant, *i.p.* administered ACBI3 induced regressions *in vivo* in the $KRAS^{G12V}$ $TP53^{R175H}$ mutant RKN xenograft model (Fig. 4L). Of note, a daily dose of 180 mg/kg of BI-2493 also induced

regressions in this model (Fig. 4L). Together these data provide first pre-clinical therapeutic proof-of-concept for pan-KRAS degradation.

Conclusion

Activating mutations in KRAS are prevalent in patients suffering from solid tumours with unmet medical need. For example, 35% of lung, 45% of colorectal, and up to 90% of pancreatic cancers are associated with KRAS mutations (*2*). This amounts to an incidence of approximately 150 000 new cases in the United States for these three tumor types (*28*). An inherent challenge to targeting KRAS with small molecules is the wide range of mutations leading to oncogenic activation. This in turn creates a challenge to identify small molecules that can broadly address the different mutations with potencies and exposures required for clinical efficacy. Despite intense research investment over decades, so far only allele specific inhibitors have been approved and the need for potent KRAS selective targeting concepts with broad mutation coverage remains high.

Here, we establish degradation of a broad spectrum of oncogenic KRAS variants with a single agent achieving potent and long-lasting suppression of oncogenic signaling *in vitro* and *in vivo*. ACBI3 is a selective, potent and *in vivo* active pan-KRAS degrader discovered via a structure-based design approach guided by optimization of VHL:PROTAC:KRAS ternary complex stability and durability. This optimization allowed us to achieve a degrader that effectively acts on the majority of KRAS mutants with high prevalence in cancer patients, and as a result inhibits proliferation in KRAS mutant cell lines covering a wide range of tumor types. KRAS degradation via ubiquitin ligase recruitment enables a greater than 10-fold higher potency compared to target inhibition and results in prolonged suppression of MAPK signaling. ACBI3 is a first example of a single agent capable of selectively degrading a major share of highly prevalent oncogenic KRAS variants. We also establish that ACBI3 suppresses oncogenic KRAS protein levels *in vivo* beyond its pharmacokinetic presence, ultimately resulting in tumor regression. Identifying approaches to dose ACBI3 safely in mice qualifies this molecule for use in preclinical *in vivo* tumor models. Bifunctional degraders rely on engaging the E3 ligase machinery with a dedicated binding motif which may be associated with ubiquitin proteasome system related resistance mechanisms (*29*) and increased efflux liability (*30*). However, the demonstrated ability of ACBI3 to potently target a wide spectrum of KRAS variants opens up opportunities for degraders to address susceptibility to resistance associated with on-target KRAS mutations. ACBI3 illustrates many key features specific to degraders made of reversible target binders, such as catalytic mode of action independent of occupancy driven pharmacology. This more broadly suggests fundamental advantages for targeting a spectrum of chemically heterogenous disease-relevant protein variants by targeted protein degradation. We anticipate that pan-KRAS degradation will deliver a new path to address a broad sweep of malignancies with high unmet medical need.

Fig. 1

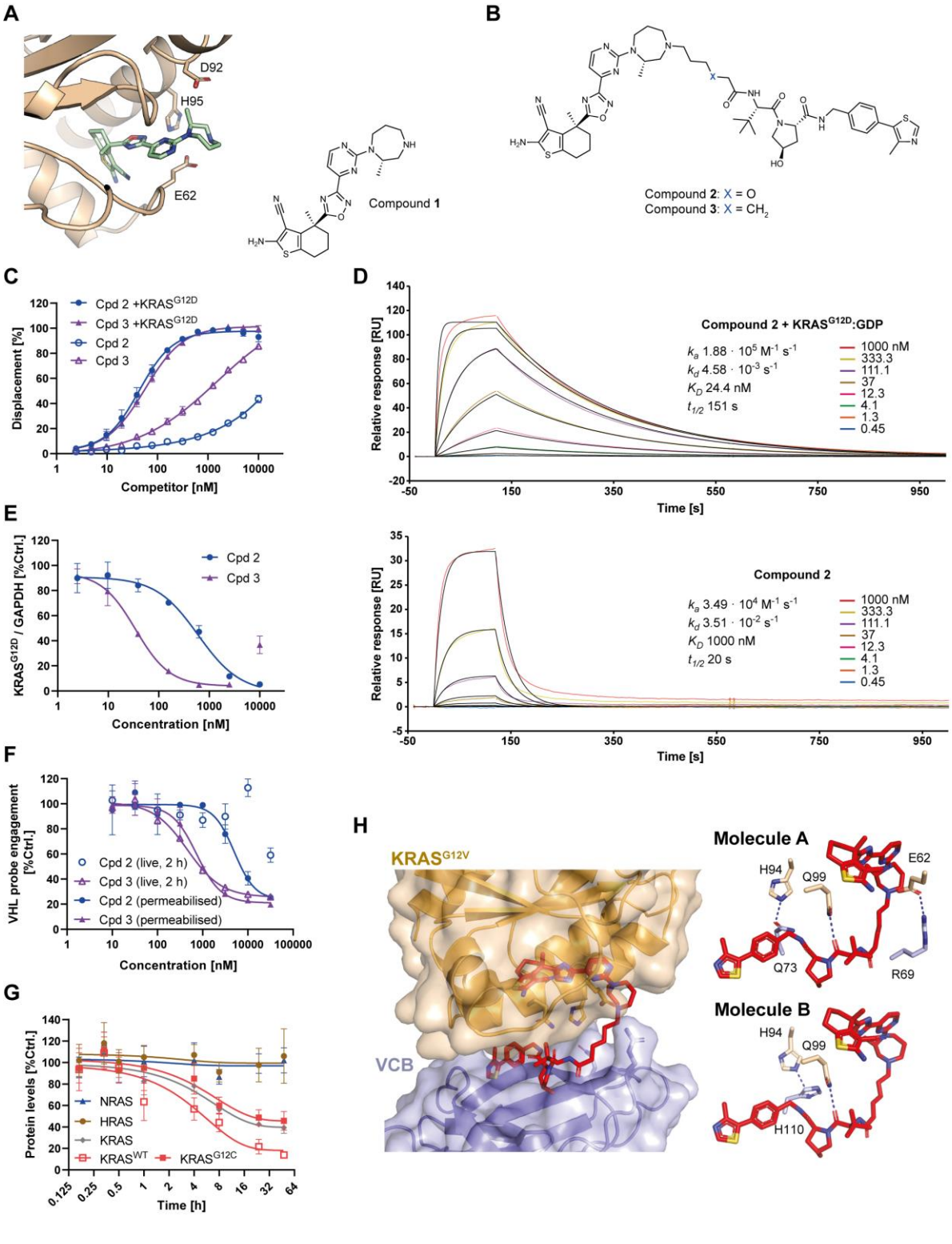
A
D92
H95
E62
Compound 1
B
Compound 2: X = O
Compound 3: X = CH2
C
Cpd 2 +KRASG12D
Cpd 3 +KRASG12D
Cpd 2
Cpd 3
Displacement [%]
Competitor [nM]
D
Compound 2 + KRASG12D:GDP
ka 1.88 · 10^5 M^-1 s^-1
kd 4.58 · 10^-3 s^-1
KD 24.4 nM
t1/2 151 s
1000 nM
333.3
111.1
37
12.3
4.1
1.3
0.45
Relative response [RU]
Time [s]
Compound 2
ka 3.49 · 10^4 M^-1 s^-1
kd 3.51 · 10^-2 s^-1
KD 1000 nM
t1/2 20 s
E
KRASG12D / GAPDH [%Ctrl.]
Concentration [nM]
F
VHL probe engagement [%Ctrl.]
Cpd 2 (live, 2 h)
Cpd 3 (live, 2 h)
Cpd 2 (permeabilised)
Cpd 3 (permeabilised)
G
Protein levels [%Ctrl.]
NRAS
HRAS
KRAS
KRASWT
KRASG12C
Time [h]
H
KRASG12V
VCB
Molecule A
H94
Q99
E62
Q73
R69
Molecule B
H110

Fig. 1. Identification of reversible, KRAS selective degraders. (**A**) Exit vector explored to derivatise KRAS-binders. Three-dimensional crystal structure of KRAS displayed in brown, compound 1 in green. PDB Accession code 8QUG. (**B**) Chemical structures of compound **2** and -**3**. (**C**) VCB FP displacement for compounds **2** and -**3** in presence or absence of saturating $KRAS^{G12D}$ concentrations (N=3, SD). (**D**) SPR characterization of ternary complex for VCB, $KRAS^{G12D}$:GDP and compound **2** (N=3, representative trace). (**E**) Dose-dependent degradation of $KRAS^{G12D}$ in GP5d cells by capillary electrophoresis (24 hours, N=3, SD). (**F**) VHL target engagement by NanoBRET in live or permeabilized HEK293 cells for compounds **2** and -**3** (N=3, SD). (**G**) Degradation time course of total KRAS, $KRAS^{WT}$, $KRAS^{G12C}$, H- and NRAS by 1 µM compound **3** in NCI-H358 cells (N=3, SD) by targeted proteomics. (**H**) Ternary complex co-crystal structure of VCB: compound **3**:$KRAS^{G12V}$.

Fig. 2

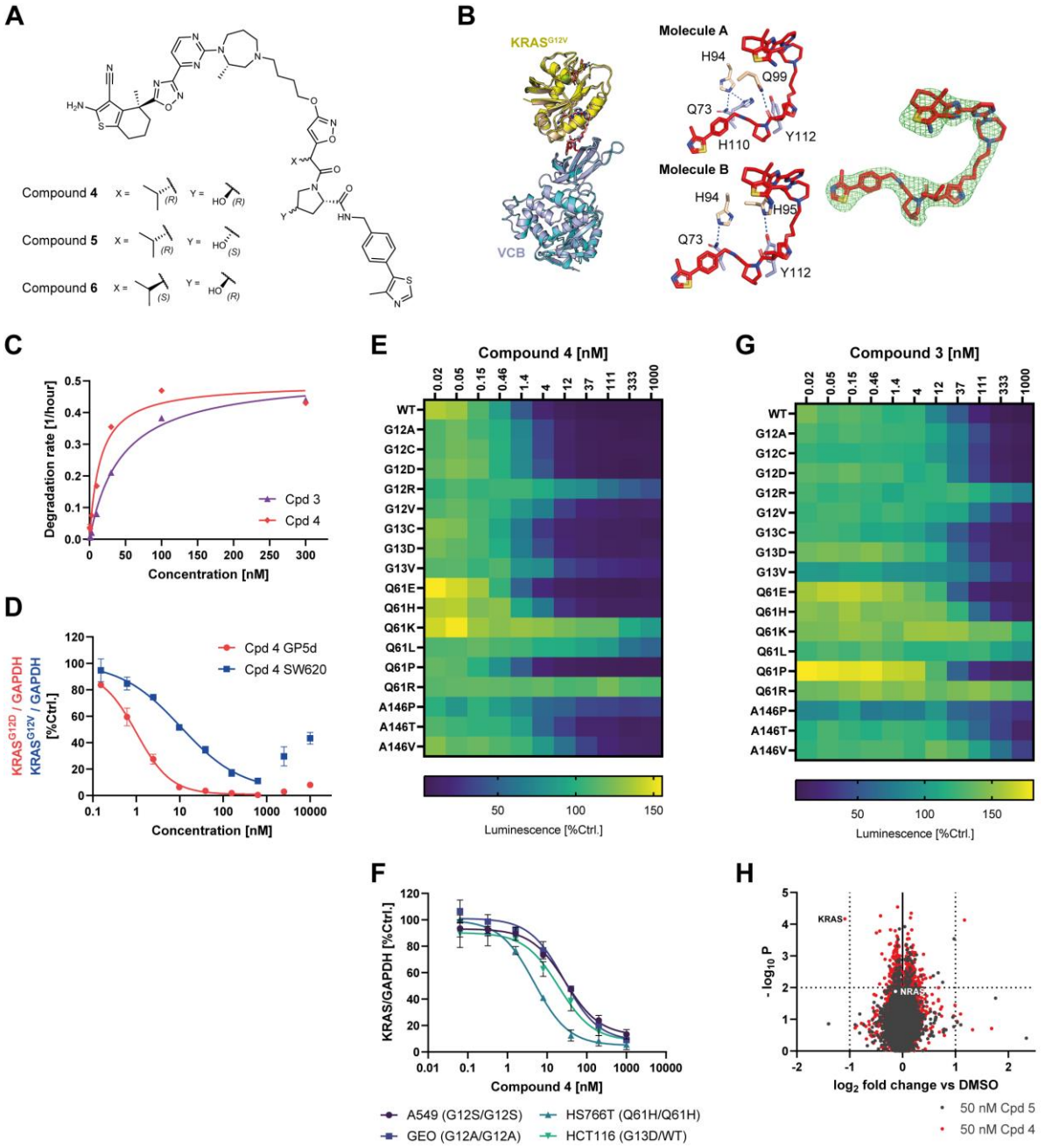

Fig. 2. Targeting of all major oncogenic KRAS alleles and sustained pathway engagement with rapid degraders. (**A**) Chemical structures of compound **4** and inactive degrader controls compound **5** ((*S*)-hydroxyproline derivative compound **4**) and -**6** ((*S*)-isopropyl). (**B**) Left: superposition of ternary complex structures of compound **3** (red):VCB (light blue):KRAS^{G12V} (wheat), and compound **4** (white):VCB (teal):KRAS^{G12V} (yellow) displaying conserved ternary binding orientations (RMSD = 0.72 Å). Middle: views from the compound 4 ternary complex PROTAC binding sites (molecules A and B) displaying side chains of residues involved in potential strong protein:protein interactions (blue dotted lines). Right: Fo-Fc omit map contoured to 3 σ for compound **4**. (**C**) Concentration dependency of degradation rates for compound **3** and compound **4** in HiBiT-tagged GP5d cells (N=6, mean±95% CI). (**D**) Dose-dependent degradation of KRAS^{G12D} and KRAS^{G12V} in GP5d and SW260 cells, respectively by capillary electrophoresis (24 hours, N=3, SD). (**E**) Degradation of retrovirally transduced HiBiT-tagged indicated KRAS mutants by compound **4** in GP5d

cells (18 hours, N=3) (**F**) Dose-dependent degradation of $KRAS^{G12S}$, $KRAS^{G12A}$, $KRAS^{G13D}$ and $KRAS^{Q61H}$ in A549, GEO, HCT116 and HS766T cells, respectively, by capillary electrophoresis (24 hours, N=3, SD). (**G**) Degradation of retrovirally transduced HiBiT-tagged indicated KRAS mutants by compound **3** in GP5d cells (18 hours, N=2) (**H**) Whole cell proteomics MS analysis of GP2d cells treated with 50 nM compound **4** or inactive stereoisomer compound **5** (8 hours, N=3) data for NRAS and compound **4** highlighted in white.

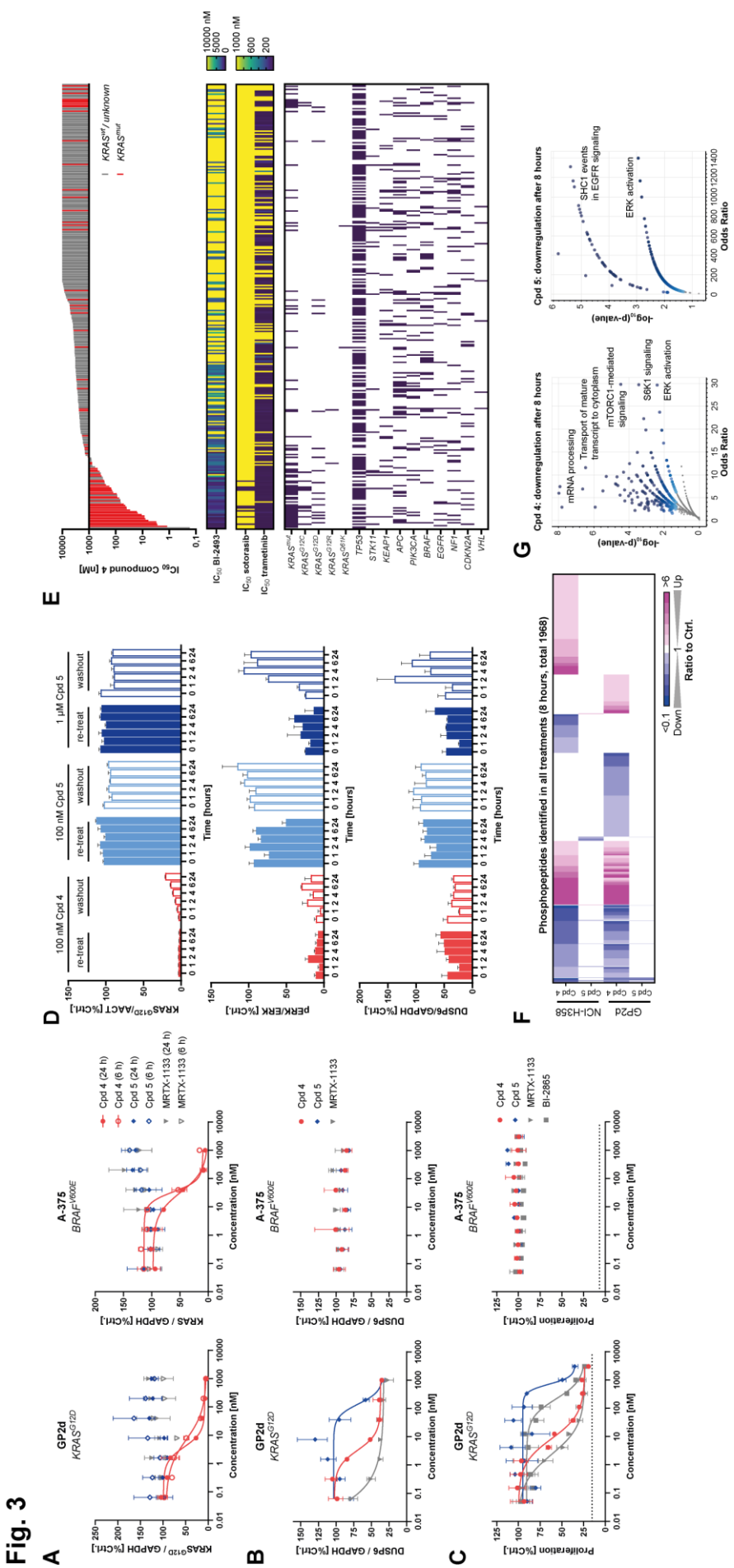
Fig. 3
A
B
C
D
E
F
G
GP2d
KRASG12D
A-375
BRAFV600E
Concentration [nM]
Cpd 4 (24 h)
Cpd 4 (6 h)
Cpd 5 (24 h)
Cpd 5 (6 h)
MRTX-1133 (24 h)
MRTX-1133 (6 h)
Cpd 4
Cpd 5
MRTX-1133
Bi-2865
KRASG12D / GAPDH [%Ctrl.]
DUSP6 / GAPDH [%Ctrl.]
Proliferation [%Ctrl.]
100 nM Cpd 4
100 nM Cpd 5
1 µM Cpd 5
re-treat
washout
Time [hours]
KRASG12D/AACT [%ctrl.]
pERK/tERK [%ctrl.]
DUSP6/GAPDH [%ctrl.]
IC50 Compound 4 [nM]
IC50 Bi-2493
IC50 sotorasib
IC50 trametinib
KRASwt / unknown
KRASmut
KRASwt
KRASG12C
KRASG12D
KRASG12R
KRASG61H
TP53
STK11
KEAP1
APC
PIK3CA
BRAF
EGFR
NF1
CDKN2A
VHL
Phosphopeptides identified in all treatments (8 hours, total 1968)
GP2d
NCI-H358
Cpd 5
Cpd 4
Down
Up
Ratio to Ctrl.
Cpd 4: downregulation after 8 hours
Cpd 5: downregulation after 8 hours
mRNA processing
Transport of mature transcript to cytoplasm
mTORC1-mediated signaling
S6K1 signaling
ERK activation
SHC1 events in EGFR signaling
-log10(p-value)
Odds Ratio

Fig. 3. Pan-KRAS degradation impacts MAPK signaling and cancer cell proliferation. (**A**) KRAS degradation (6 and 24 hours, N=2, range), (**B**) *DUSP6* modulation (6 hours, N=3, SD), (**C**) proliferation (5 days, N=3, SD) for compound **4**, compound **5** and MRTX1133 in $KRAS^{G12D}$ and $BRAF^{V600E}$ cell lines, respectively. (**D**) $KRAS^{G12D}$, pERK and DUSP6 recovery in GP2d cells upon re-treatment or washout and VHL competition following 18 hours pre-treatment with compound **4** or compound **5** (time after washout, N=3, SD). (**E**) Proliferation inhibition data for 300 cancer cell lines by compound **4** (bars represent IC_{50} per cell line), BI-2493 (*6*), sotorasib or trametinib (heatmap) (5 days, N=3) including genetic features of tested cell lines. (**F**) Heat map of phosphorylation events upon treatment with compound **4** or compound **5** in NCI-H358 ($KRAS^{G12C}$, 500 nM) and GP2d ($KRAS^{G12D}$, 100 nM) cells (8 hours, N=3). (**G**) Volcano plots of combined gene set enrichment analyses of phospho-proteome changes induced by compound **4** (upper panel) or compound **5** (lower panel) in NCI-H358 and GP2d cells at 8 hours.

Fig. 4

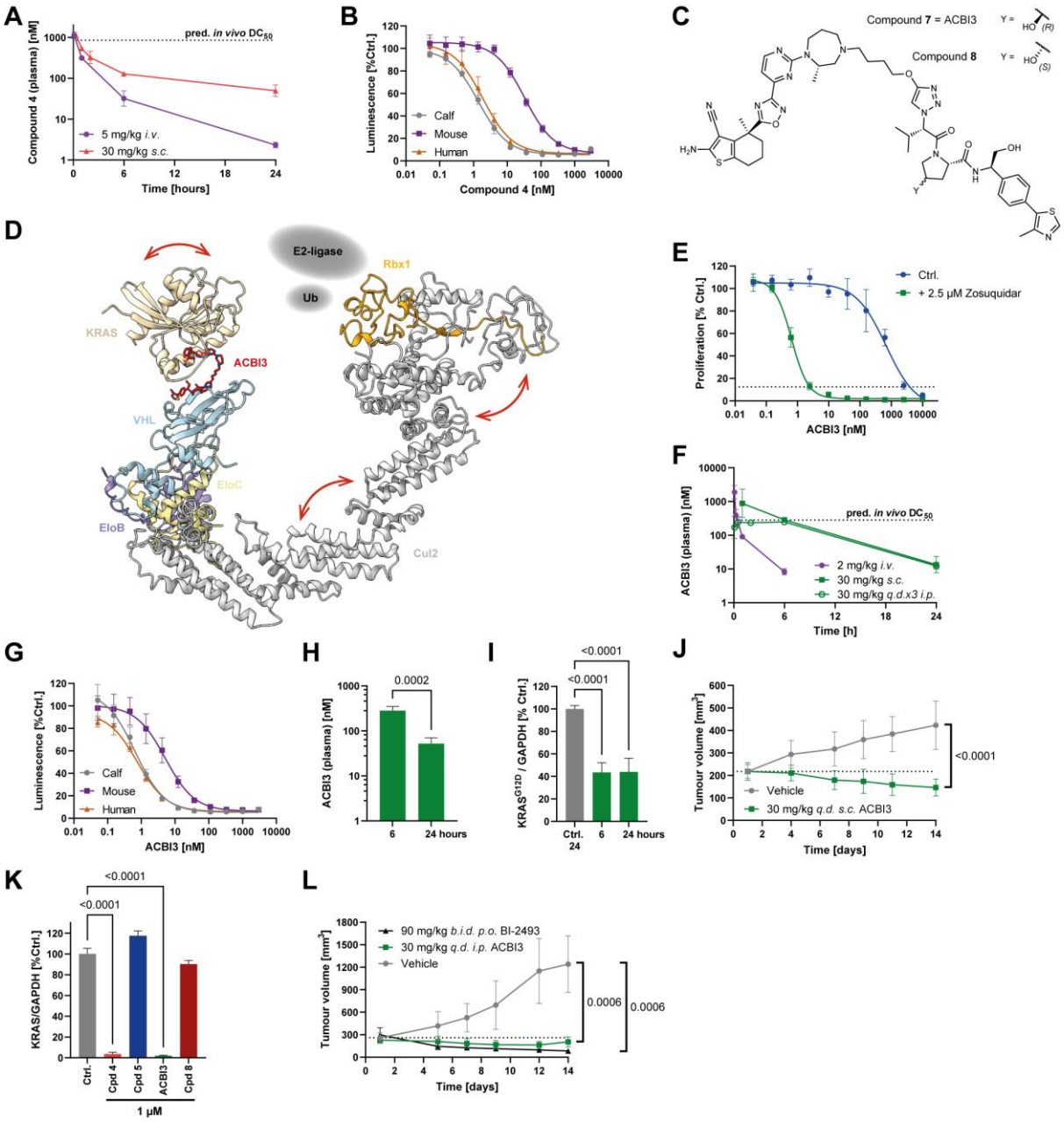

Fig. 4. *In vivo* efficacy associated with degradation of KRAS^{G12D} and KRAS^{G12V}. (**A**) Pharmacokinetic profile of compound **4** in mice upon *i.v.* or *s.c.* dosing, 2-hydroxypropyl-β-cyclodextrin (HP-β-CD) formulation (N=3, geometric mean and geometric SD). (**B**) Degradation of HiBiT-KRAS^{G12D} (24 hours, N=4, SD) by compound **4** in GP5d cells in presence of 10% fetal calf, mouse or human serum. (**C**) Chemical structure of ACBI3. (**D**) Cryo-EM structure of the KRAS:ACBI3:VCB:Cul2:Rbx1 heptameric complex, major motions indicated as red arrows (Cul2 breathing, KRAS rocking and Rbx1 twisting), expected positions of the E2-ligase and ubiquitin added schematically in dotted ellipses. (**E**) Proliferation of ACBI3 in LS513 cells in presence and absence of 2.5 µM Zosuquidar (5 days, N=3). (**F**) Pharmacokinetic profile of ACBI3 in mice upon *i.v.* (HP- β-CD), *s.c.* or *q.d.x3 i.p.* dosing (N=3, geometric mean and geometric SD). (**G**) Degradation of HiBiT-KRAS^{G12D} (24 hours, N=4, SD) in GP5d cells in presence of 10% fetal calf-, mouse- or human serum. (**H**) ACBI3 plasma levels in subcutaneous GP2d tumor bearing mice dosed with 30 mg/kg ACBI3 *q.d.x3* (N=5, geometric mean and geometric SD, Welch's t-test). (**I**) *In*

vivo degradation of $KRAS^{G12D}$ upon *s.c. q.d.x3* dosing of 30 mg/kg ACBI3. (N=5, mean and SD). (**J**) *In vivo* efficacy of ACBI3 in a GP2d xenograft model (N=10, mean and SD, Wilcoxon test). (**K**) *In vitro* degradation of murine KRAS in B16F10 cells by 1 µM compound **4**, ACBI3 and corresponding inactive stereoisomers compound **5** and -**8** by capillary electrophoresis (24 hours, N=3, mean and SD, One-way ANOVA, Dunnet correction). (**L**) *In vivo* efficacy of ACBI3 in a RKN xenograft model (N=7, mean and SD, Wilcoxon text day 14 (N=4 control-, N=7 treatment groups).

References and Notes:

1. F. Skoulidis *et al.*, Sotorasib for Lung Cancers with KRAS p.G12C Mutation. *N Engl J Med* **384**, 2371-2381 (2021).
2. L. Herdeis, D. Gerlach, D. B. McConnell, D. Kessler, Stopping the beating heart of cancer: KRAS reviewed. *Curr Opin Struct Biol* **71**, 136-147 (2021).
3. L. Huang, Z. Guo, F. Wang, L. Fu, KRAS mutation: from undruggable to druggable in cancer. *Signal Transduct Target Ther* **6**, 386 (2021).
4. S. I. Ou *et al.*, First-in-Human Phase I/IB Dose-Finding Study of Adagrasib (MRTX849) in Patients With Advanced KRAS(G12C) Solid Tumors (KRYSTAL-1). *J Clin Oncol* **40**, 2530-2538 (2022).
5. X. Wang *et al.*, Identification of MRTX1133, a Noncovalent, Potent, and Selective KRAS(G12D) Inhibitor. *J Med Chem* **65**, 3123-3133 (2022).
6. D. Kim *et al.*, Pan-KRAS inhibitor disables oncogenic signalling and tumour growth. *Nature* **619**, 160-166 (2023).
7. W. Farnaby, M. Koegl, D. B. McConnell, A. Ciulli, Transforming targeted cancer therapy with PROTACs: A forward-looking perspective. *Curr Opin Pharmacol* **57**, 175-183 (2021).
8. D. Chirnomas, K. R. Hornberger, C. M. Crews, Protein degraders enter the clinic - a new approach to cancer therapy. *Nat Rev Clin Oncol* **20**, 265-278 (2023).
9. M. Zeng *et al.*, Exploring Targeted Degradation Strategy for Oncogenic KRAS(G12C). *Cell Chem Biol* **27**, 19-31 e16 (2020).
10. M. J. Bond, L. Chu, D. A. Nalawansha, K. Li, C. M. Crews, Targeted Degradation of Oncogenic KRAS(G12C) by VHL-Recruiting PROTACs. *ACS Cent Sci* **6**, 1367-1375 (2020).
11. D. P. Bondeson *et al.*, Catalytic in vivo protein knockdown by small-molecule PROTACs. *Nat Chem Biol* **11**, 611-617 (2015).
12. A. P. Tolcher, W.; Wang, J.S.; Spira, A.; Janne, P.; Lee, H.; Gill, S.; LoRusso, P.; Herzberg, B.; Goldman, J.: Morgensztern, D.; Berlin, J.; Kasi, A.; Fujii, H.; Pelster, M., Trial in progress: A phase 1, first-in-human, open-label, multicenter, dose-escalation and dose-expansion study of ASP3082 in patients with previously treated advanced solid tumors and KRAS G12D mutations. *J Clin Oncol* **41**, Suppl 4 (2023).
13. J. Broker *et al.*, Fragment Optimization of Reversible Binding to the Switch II Pocket on KRAS Leads to a Potent, In Vivo Active KRAS(G12C) Inhibitor. *J Med Chem* **65**, 14614-14629 (2022).
14. C. Galdeano *et al.*, Structure-guided design and optimization of small molecules targeting the protein-protein interaction between the von Hippel-Lindau (VHL) E3 ubiquitin ligase and the hypoxia inducible factor (HIF) alpha subunit with in vitro nanomolar affinities. *J Med Chem* **57**, 8657-8663 (2014).
15. M. S. Gadd *et al.*, Structural basis of PROTAC cooperative recognition for selective protein degradation. *Nat Chem Biol* **13**, 514-521 (2017).
16. M. K. Schwinn *et al.*, CRISPR-Mediated Tagging of Endogenous Proteins with a Luminescent Peptide. *ACS Chem Biol* **13**, 467-474 (2018).
17. T. A. Soucy *et al.*, An inhibitor of NEDD8-activating enzyme as a new approach to treat cancer. *Nature* **458**, 732-736 (2009).
18. J. Frost *et al.*, Potent and selective chemical probe of hypoxic signalling downstream of HIF-alpha hydroxylation via VHL inhibition. *Nat Commun* **7**, 13312 (2016).
19. M. J. Roy *et al.*, SPR-Measured Dissociation Kinetics of PROTAC Ternary Complexes Influence Target Degradation Rate. *ACS Chem Biol* **14**, 361-368 (2019).
20. P. S. Dragovich *et al.*, Antibody-Mediated Delivery of Chimeric BRD4 Degraders. Part 2: Improvement of In Vitro Antiproliferation Activity and In Vivo Antitumor Efficacy. *J Med Chem* **64**, 2576-2607 (2021).

21. S. Imaide *et al.*, Trivalent PROTACs enhance protein degradation via combined avidity and cooperativity. *Nat Chem Biol* **17**, 1157-1167 (2021).
22. D. L. Buckley *et al.*, Targeting the von Hippel-Lindau E3 ubiquitin ligase using small molecules to disrupt the VHL/HIF-1alpha interaction. *J Am Chem Soc* **134**, 4465-4468 (2012).
23. J. Canon *et al.*, The clinical KRAS(G12C) inhibitor AMG 510 drives anti-tumour immunity. *Nature* **575**, 217-223 (2019).
24. J. Hallin *et al.*, Anti-tumor efficacy of a potent and selective non-covalent KRAS(G12D) inhibitor. *Nat Med* **28**, 2171-2182 (2022).
25. A. Mares *et al.*, Extended pharmacodynamic responses observed upon PROTAC-mediated degradation of RIPK2. *Commun Biol* **3**, 140 (2020).
26. D. L. Slate *et al.*, RS-33295-198: a novel, potent modulator of P-glycoprotein-mediated multidrug resistance. *Anticancer Res* **15**, 811-814 (1995).
27. S. M. Shah, A. S. Jain, R. Kaushik, M. S. Nagarsenker, M. J. Nerurkar, Preclinical formulations: insight, strategies, and practical considerations. *AAPS PharmSciTech* **15**, 1307-1323 (2014).
28. P. H. Viale, The American Cancer Society's Facts & Figures: 2020 Edition. *J Adv Pract Oncol* **11**, 135-136 (2020).
29. P. Ottis *et al.*, Cellular Resistance Mechanisms to Targeted Protein Degradation Converge Toward Impairment of the Engaged Ubiquitin Transfer Pathway. ACS Chem Biol **14**, 2215-2223 (2019).
30. C. Kofink *et al.*, A selective and orally bioavailable VHL-recruiting PROTAC achieves SMARCA2 degradation in vivo. *Nat Commun* 13, 5969 (2022).
31. W. Farnaby *et al.*, BAF complex vulnerabilities in cancer demonstrated via structure-based PROTAC design. *Nat Chem Biol* **15**, 672-680 (2019).
32. D. Kessler *et al.*, Drugging an undruggable pocket on KRAS. *Proc Natl Acad Sci U S A* **116**, 15823-15829 (2019).
33. C. Vonrhein *et al.*, Data processing and analysis with the autoPROC toolbox. *Acta Crystallogr D Biol Crystallogr* **67**, 293-302 (2011).
34. A. J. McCoy *et al.*, Phaser crystallographic software. *J Appl Crystallogr* **40**, 658-674 (2007).
35. P. Emsley, B. Lohkamp, W. G. Scott, K. Cowtan, Features and development of Coot. *Acta Crystallogr D Biol Crystallogr* **66**, 486-501 (2010).
36. D. Liebschner *et al.*, Macromolecular structure determination using X-rays, neutrons and electrons: recent developments in Phenix. *Acta Crystallogr D Struct Biol* **75**, 861-877 (2019).
37. J. Agirre *et al.*, The CCP4 suite: integrative software for macromolecular crystallography. *Acta Crystallogr D Struct Biol* **79**, 449-461 (2023).
38. A. Punjani, J. L. Rubinstein, D. J. Fleet, M. A. Brubaker, cryoSPARC: algorithms for rapid unsupervised cryo-EM structure determination. *Nat. Methods* **14**, 290–296 (2017).
39. A. Punjani, D. J. Fleet, 3D variability analysis: Resolving continuous flexibility and discrete heterogeneity from single particle cryo-EM. *J. Struct. Biol.* **213**, 107702 (2021).
40. A. Punjani, D. J. Fleet, 3DFlex: determining structure and motion of flexible proteins from cryo-EM. *Nat. Methods* **20**, 860–870 (2023).
41. R. Sanchez-Garcia, J. Gomez-Blanco, A. Cuervo, J. M. Carazo, C. O. S. Sorzano, J. Vargas, DeepEMhancer: a deep learning solution for cryo-EM volume post-processing. *Commun Biology* **4, 874** (2021).
42. T. A. F. Cardote, M. S. Gadd, A. Ciulli, Crystal Structure of the Cul2-Rbx1-EloBC-VHL Ubiquitin Ligase Complex. *Structure* **25**, 901-911 e903 (2017).

43. E. F. Pettersen *et al.*, UCSF ChimeraX: Structure visualization for researchers, educators, and developers. *Protein Sci* **30**, 70-82 (2021).
44. A. Testa, S. J. Hughes, X. Lucas, J. E. Wright, A. Ciulli, Structure-Based Design of a Macrocyclic PROTAC. *Angew Chem Int Ed Engl* **59**, 1727-1734 (2020).
45. Y. Cui *et al.*, A Bidirectional Permeability Assay for beyond Rule of 5 Compounds. *Pharmaceutics* **13**, (2021).
46. J. Zecha *et al.*, Decrypting drug actions and protein modifications by dose- and time-resolved proteomics. *Science* **380**, 93-101 (2023).
47. E. Y. Chen *et al.*, Enrichr: interactive and collaborative HTML5 gene list enrichment analysis tool. *BMC Bioinformatics* **14**, 128 (2013).
48. W. Liebermeister *et al.*, Visual account of protein investment in cellular functions. *Proc Natl Acad Sci U S A* **111**, 8488-8493 (2014).
49. D. J. Rigden, X. M. Fernandez, The 2022 Nucleic Acids Research database issue and the online molecular biology database collection. *Nucleic Acids Res* **50**, D1-D10 (2022).
50. D. K. Schweppe *et al.*, Full-Featured, Real-Time Database Searching Platform Enables Fast and Accurate Multiplexed Quantitative Proteomics. J Proteome Res **19**, 2026-2034 (2020).

Acknowledgments:

We would like to acknowledge technical and experimental support by Géraldine Garavel, Peter Greb, Karin Stefanie Hofbauer, Christoph Peinsipp, Yvonne Scherbantin, Florian Schiel (chemical syntheses), Sandra Doebel, Michael Galant, and Patrick Werni (molecular cloning, protein production and purification of KRAS proteins), Aldina Crnic, Simone Lieb, Corinna Melichar, Ana Orsolic (cellular biology assays), James Habineza, Sonja Porits, Katrin Gitschtaler (in vivo pharmacology), Nina Braun and Romy Schopper (Cellular assay support), Bernadette Sharps, Thomas Gerstberger and Niklas Baumann (Biochemical assay support), Klaus Rumpel (biophysics assay support), Ines Truebenbach, Ida Dinold, Philipp Toplak (formulation development), Angelika Hörschläger (targeted proteomics) - all from Boehringer-Ingelheim. We acknowledge Abdel Atrih and Douglas Lamont from the University of Dundee FingerPrint Proteomics facility for support with mass spectrometry proteomics. We also acknowledge Dario Alessi from MRC PPU, University of Dundee, for the gift of mouse embryonic fibroblasts.

Funding:

We thank European Synchrotron Radiation Facility and Diamond Light Source for beamtime (BAG proposal MX14980) and for support at beamlines I23-1 and I24 respectively. This work has received funding from Boehringer Ingelheim and the Austrian Promotion Agency (grant numbers 871904 and 900397). Biophysics and drug discovery and proteomics/computing activities at Dundee were partially supported by Wellcome Trust strategic awards (100476/Z/12/Z, 094090/Z/10/Z and 097945/C/11/Z respectively).

Author contributions:

J.P., W.F., C.K. and A.G. contributed equally and will be putting their name first on the citation in their CVs. A.C. and P.E. co-conceived the study, designed and supervised experiments and co-wrote the paper. J.P. and W.F. designed, analysed and supervised experiments, prepared figures and co-wrote the paper. C.K. and A.G. designed compounds and synthetic routes and co-wrote the paper. E.D., A.B.F., J.G.-T., R.M., N.T., H.W. and S.Z. designed compounds and synthetic routes. J. K-O., T.K., O.P. synthesised key compounds. M.K. co-wrote the manuscript. G.F., S.A-S., D.P. and P. S-B. contributed to production and analysis of cryo-EM data. R.K. performed small molecule structure identification and analysis. B.K., P.P., C.H. and A.L. designed and performed phosphoproteomics studies. B.K.

produced binary X-ray structures. A.W. and D.Z. crystallised ternary complexes KRAS:PROTAC:VCB and determined their co-crystal structures. K.K. and A.W. designed and performed biophysical assays. S.K., C.W., V.V., S.O. and V.R., designed, interpreted and performed cellular assays. R.M. and V.V. designed, analysed and performed proteomics studies. N.M. designed and interpreted targeted proteomics and co-wrote the manuscript and N.M. and H.A. designed in vivo PK and in vitro ADME studies. M.W., P.S., E.S., S.B. and G.B. designed and interpreted in vivo studies and co-wrote figures. J.Q. measured effects of P-gp substrate properties on cancer cell line panel data.

Competing interests:

J.P., A.G., C.K., G.F., M.W., N.M., C.H., H.A., S.A-S., S.B., G.B., J.K-O., T.K., M.K., R.K., B.K., K.K., A.A.L, S.O., D.P., O.P., V.R., P.S-B., P.S., E.S., J.Q., H.W., P.E. are current or former employees of Boehringer Ingelheim. A.C. is a scientific founder, shareholder and advisor of Amphista Therapeutics, a company that is developing targeted protein degradation therapeutic platforms. The Ciulli laboratory receives or has received sponsored research support from Almirall, Amgen, Amphista Therapeutics, Boehringer Ingelheim, Eisai, Merck KaaG, Nurix Therapeutics, Ono Pharmaceuticals and Tocris-Biotechne.

Data and materials availability:

Atomic coordinates and structure factors for X-ray crystallographic and cryo-electron microscopy structures have been deposited in the Protein Data Bank (and the EMDB) with accession codes 8QUG, 8QU8 (EMD-18657), 8QW6, 8QW7 and 8QVU. All raw data and search results for proteomics studies have been deposited to the ProteomeXchange Consortium with the dataset identifiers PXD046161, PXD045416 and PXD045460, respectively.

Supplementary Materials:

Materials and Methods

Figs. S1 to S8

Tables S1 to S6

Chemical synthesis procedures

ACBI3 proliferation data